Supporting Information

In-situ construction of static-dynamic hybrid interface toward stable Zn anode for aqueous Zn-ion batteries

Baohua Liu,[a] Luyan Yu,[a] Qinghua Xiao,[a] Shilin Zhang*[b], Guanjie Li,[b] Kaixin Ren,[a] Yuxuan Zhu,[a] Chao Wang*[a]and Qinghong Wang*[a]

[a]*School of Chemistry and Materials Science, Jiangsu Normal University, Xuzhou, Jiangsu 221116, P. R. China.*
[b]*School of Chemical Engineering, Faculty of Sciences, Engineering and Technology, The University of Adelaide, Adelaide, SA 5005, Australia.*
**Corresponding author. E-mail: shilin.zhang01@adelaide.edu.au (S. Zhang), wangc@jsnu.edu.cn (C. Wang), wangqh@jsnu.edu.cn (Q. Wang)*

Experimental Section

Chemicals Experimental Details: Zinc sulfate heptahydrate ($ZnSO_4 \cdot 7H_2O$, 99.995%) was purchased from Shanghai Titan Scientific Co., Ltd.Trolamine($C_6H_{15}NO_3$, AR) was purchased from Shanghai Aladdin Biochemical Technology Co. Ltd. Zn foil (10 and 30 μm, 99.9%), Cu foil, and glass fiber (0.96 mm) were purchased from Shenzhen Kejing Star Technology.

Experiment preparation: Electrolyte preparation: A certain volume of TEA was dissolved in 2.0 mol L^{-1} $ZnSO_4$ solution to prepare TEA-based electrolytes with volume fractions of 0.5 %, 1.0 % and 3.0 %, respectively, named TEA-0.5 %, TEA-1.0 % and TEA-3.0 %. The 2.0 mol L^{-1} $ZnSO_4$ electrolyte was named blank electrolyte (Blank electrolyte).

Cathode preparation: V_2O_5 powder, conductive carbon and polytetrafluoroethylene (PTFE) were mixed evenly at a weight ratio of 7:2:1, and anhydrous ethanol was used as a dispersant. The PTFE binder was fully stirred to form a slurry. It was rolled into a uniform sheet and then cut into a sheet. The average load of the active material was about 2.0 mg cm^{-2}.

Battery assembly: When assembling the battery, it is assembled in the order of negative shell-bullet-gasket-Zn negative electrode-diaphragm (whatman GF/D-90

mm) -positive electrode-positive shell, and the amount of electrolyte is controlled to be about 90 μL, which is added dropwise for three times.

Characterization: The morphology of zinc deposition and the distribution of elements on the electrode surface were observed by field emission electron microscopy (SEM, Hitachi SU-8010) and EDS(linked with SEM) analysis. The structure and composition of the electrode materials before and after cycling were tested by X-ray diffractometer (XRD ,Bruker-D8ADVANCE),X-ray photoelectron spectroscopy (XPS, Thermo Scientific K-Alpha+ spectrometer equipped with a monochromatic Al Kα X-ray source (1486.6 eV) operating at 100 W), Fourier Transform Infrared Spectroscopy(FTIR , Bruker VERTEX 80 v) , Atomic Force Microscopy(AFM, Bruker Dimension Icon) and Laser confocal scanning microscopy (LCSM, Carl Zeiss AG, LSM 700).The thinned sample for TEM tests was cut by a focused ion beam (FIB) and observed on the FEI Scios.

Electrochemical measurements: CR2023 coin cells were assembled to monitor the electrochemical performance of the plating/stripping process, and tested by the NEWARE battery test system (CT-4008T, Neware Technology Limited) at 25 °C. The Electrochemical Impedance Spectroscopy, (EIS), cyclic voltammetry (CV), Chronoamperometry, (CA)linear scan voltammetry(LSV), and corrosion test were conducted on an electrochemical workstation (CHI660E, Shanghai Chenhua Instrument Co. Ltd.). LSV and Tafel experiments were carried out in a three-electrode system with zinc foil as the working electrode, platinum electrode as the counter electrode and Ag/AgCl as the reference electrode. The scan rate of LSV is 10 mV s^{-1}, and the voltage range is -1.0 ~ 1.35 V. The scan rate of Tafel is 1 mV s^{-1}, and the voltage range is -0.8 ~ -1.1 V. The Electrochemical impedance spectra (EIS) were obtained in Zn||Zn symmetric cells with the frequency range of 10^{-2} Hz ~ 10^{5} Hz.

The transference number of Zn^{2+} (t_{Zn}^{2+}) was evaluated by measuring EIS before and after applied voltage of 25 mV and determined by the following equation:

$$t_{Zn^{2+}} = \frac{I_s(\Delta V - I_0 R_0)}{I_0(\Delta V - I_s R_s)}$$

(1)

where ΔV is the applied voltage (25 mV); I_0 and R_0 are the initial current and resistance, respectively; and I_S and R_S are the steady-state current and resistance, respectively.

The desolvation process of Zn^{2+} can be evaluated by the activation energy (E_a) in Arrhenius equation:

$$\frac{1}{R_{ct}} = Aexp\left(\frac{-E_a}{RT}\right) \quad (2)$$

Where Rct is the charge-transfer resistance, A is the frequency factor, R is the ideal gas constant, and T is the absolute temperature.

$$\eta_I\% = \frac{I_{corr}^{0} - I_{corr}}{I_{corr}^{0}} \times 100\% \quad (3)$$

where I_{corr}^{0} is the exchange current density of bare Zn anode, I_{corr} is the corrosion current density of modified Zn anodes.

Details for DFT calculations: DFT simulations were conducted using CP2K and ORCA to calculate the adsorption energy and binding energy, respectively .[1] Adsorption of $TEAH^+$ on ZHS were calculated using the CP2K package version-2022.1 using Gaussian Plane Wave (GPW) method implemented in the QUICKSTEP module. [2]Perdew-Burke-Ernzerhof (PBE) [3]exchange-correlation (XC) functional with Grimme-D3[4, 5] dispersion correction method was employed. Both the double-zeta valence polarized (DZVP) sets and Goedecker-Teter-Hutter (GTH) pseudopotentials were adopted [S6-S8].[6-8] Plane wave and relative cut-offs were set to 400 and 55 Ry, respectively. The inner and outer SCF convergence criteria were set to 2.0×10^{-6} Ha. In order to avoid interactions between periodic images, a vacuum distance of 20 Å was imposed between different layers. The geometrical optimizations were implemented at the *Γ* point for all surface structures. The bottom two layers of atoms

were frozen while the top two were allowed to relax. Root mean square and maximum force convergence were set to 3.0×10^{-4} and 4.5×10^{-4} Ha·Å^{-1}, respectively.

The adsorption energies were calculated according to equation (4),

$$E_{ads} = E_{(slab\ +\ adsorbate)} - E_{(slab)} - E_{(adsorbate)} \quad (4)$$

where $E_{(slab + adsorbate)}$, $E_{(slab)}$, and $E_{(adsorbate)}$ are the calculated electronic energy of species adsorbed on the surface, the bare surface, and the gas-phase molecule, respectively.

Binding energy calculations were carried out using ORCA (5.0.3). Geometry optimization was conducted at the r2SCAN-3c level of theory. [9, 10] The single point calculations for the optimized geometries were performed to obtain accurate energies at the ωB97X-V/def2-TZVP level of theory.[11-13] The solvent effect of water evaluated by the CPCM solvation model. The RIJCOSX approximation was applied with the def2/J auxiliary basis set . [14, 15]The Gibbs free energy was included in the Gibbs energy correction of unscaled vibrational analysis at the r2SCAN-3c level of theory.

The binding energy can be calculated by Equation (5), where AB represents the total energy after the binding between Zn^{2+} and the organic molecule. A and B are the energy of a single Zn^{2+} and organic molecule, respectively.

$$E_{binding} = E_{(AB)} - E_{(A)} - E_{(B)} \quad (5)$$

Details for MD simulations: MD simulations were conducted using GROMACS software package (2020.6 version). The amber99sb-ildn force field were used to parametrize all atoms, such as the bond parameters, angle parameters and the dihedral angles, and so on. The RESP charge of SO_4^{2-} and $TEAH^+$ molecule was calculated using ORCA at the B3LYP/6-311+g(d,p) level. TIP3P was used for the model of water molecule. The steepest descent method was applied to minimize the initial energy for each system with a force tolerance of 1 kJ/(mol^{-1} nm^{-1}) and a maximum step size of 0.002 ps before MD calculations. In all the three directions, periodic boundary conditions were imposed. Leapfrog algorithm was used to integrate the Newtonian equation of motion. The MD simulation was processed in an NVT ensemble and the simulation time is 15 ns at 298.15 K. The Particle-Mesh-Ewald

(PME) with a fourth-order interpolation was used to evaluate the electrostatic interactions and the grid spacing is 1.0 Å, whereas a cutoff of 1.0 Å was employed to calculate the short-range van der Waals interactions. The last frame of the above 15 ns simulation trajectory was used as the initial frame for the subsequent 15 ns NVT simulation in the presence of electric field (-1.0 V nm^{-1} along Z), which aimed to explore the adsorption of $TEAH^+$ on ZHS with electric field.

Supplementary Figures

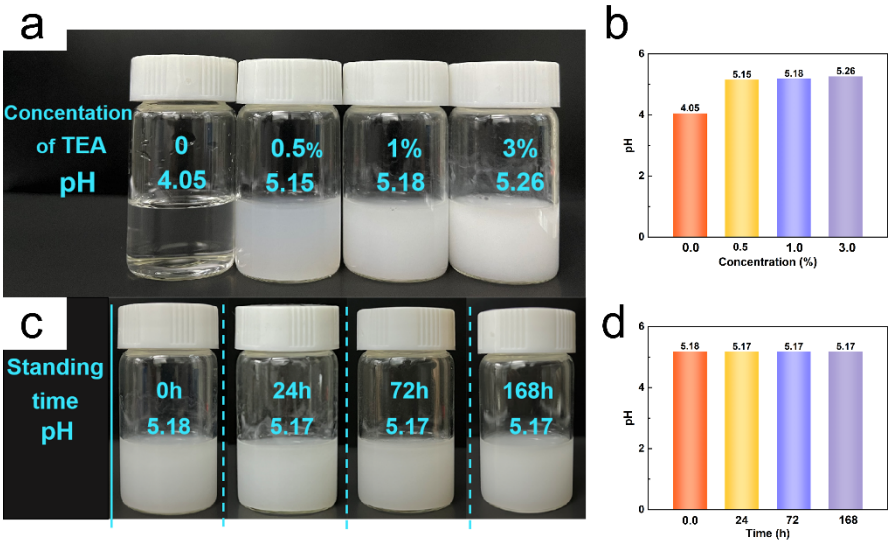

Figure S1. (a) Photos of the blank electrolyte and TEA-based electrolytes, (b) The pH values of the electrolytes with different concentrations of TEA additive, (c) Photos of TEA-based electrolytes after a certain standing time and (d) The pH values of the electrolytes after a certain standing time.

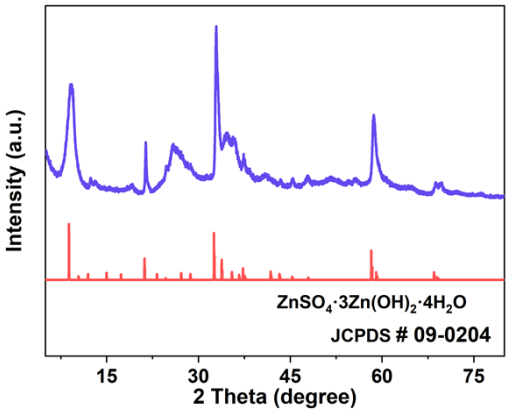

Figure S2. XRD pattern of white precipitate obtained in the TEA-based electrolyte.

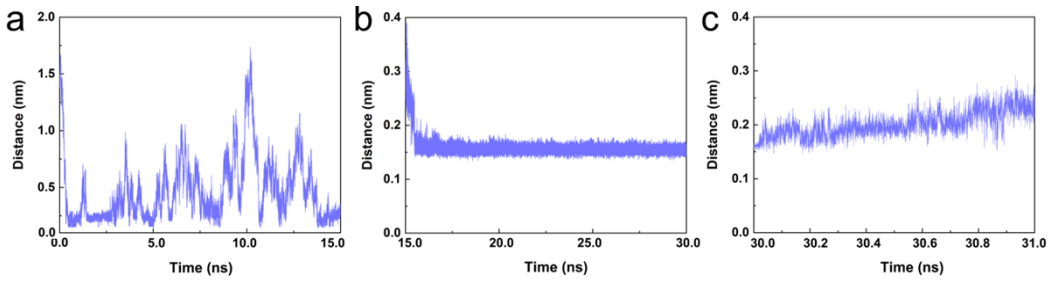

Figure S3. The minimum distance change with time between the inorganic ZHS layer and organic $TEAH^+$ (a) without electric field, (b) with negative electric field and (c) with positive electric field.

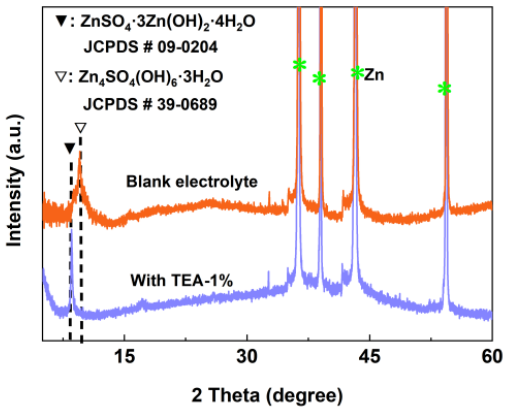

Figure S4. XRD patterns of the Zn anode after 3 cycles in blank electrolyte and in the electrolyte with TEA-1.0%.

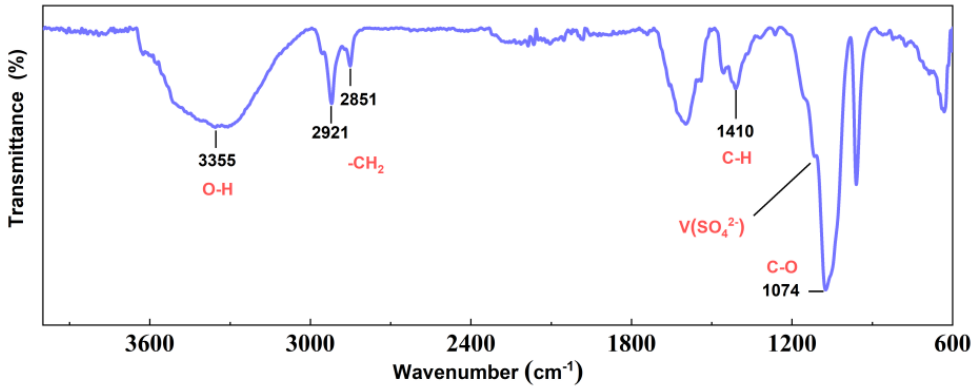

Figure S5. FT-IR spectra of the Zn anode after 5 cycles in the electrolyte with TEA.

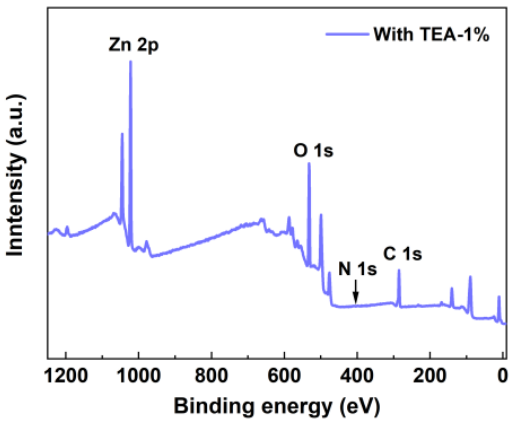

Figure S6. XPS spectra of Zn anode after the 3rd stripping/plating process with electrolyte containing TEA.

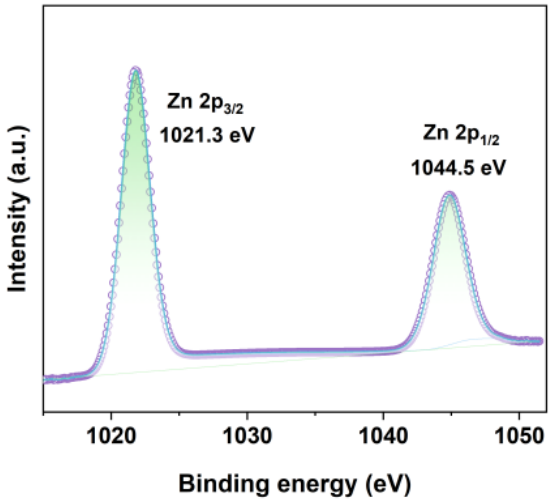

Figure S7. High resolution spectra of Zn 2p after the 3rd stripping/plating process in the electrolyte containing TEA.

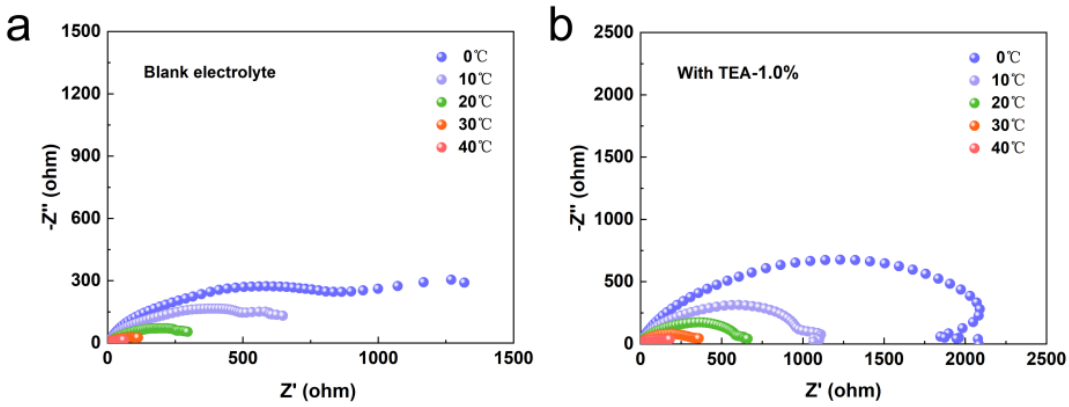

Figure S8. Nyquist plots of Zn||Zn symmetric cells testing under various temperatures in (a) the Black electrolyte and (b) with TEA electrolyte.

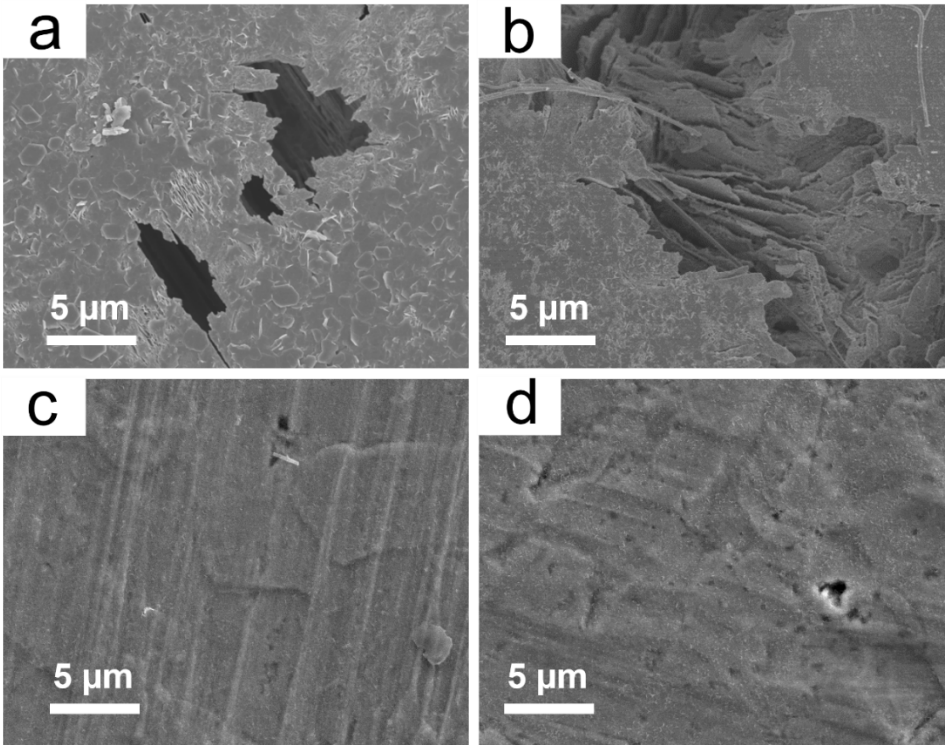

Figure S9. SEM image of the Zn anode after the 10th striping process in (a) blank electrolyte and (b) TEA-based electrolyte at the current density of 1.0 mA cm^{-2} with the areal capacity of 1.0 mAh cm^{-2}.

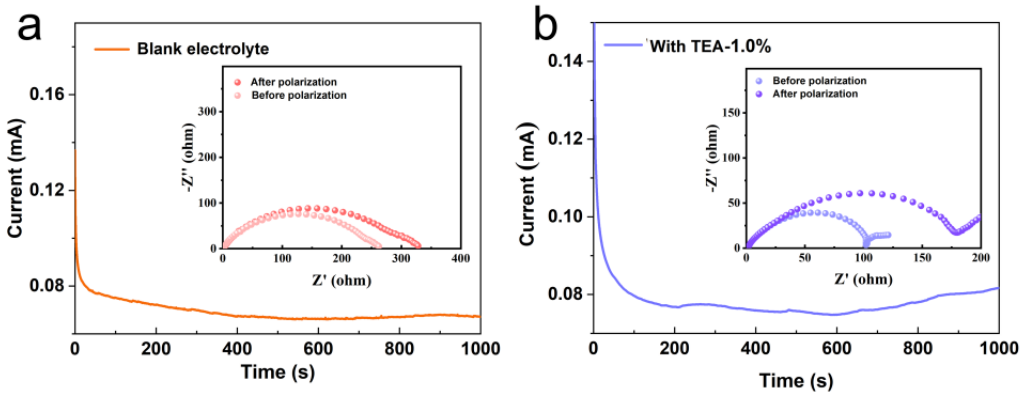

Figure S10. I-t curve of symmetric cells with (a) Black electrolyte and (b) TEA-based electrolyte at an applied voltage of 25 mV. The insets show EIS spectra before and after polarization of (a) Black electrolyte and (b) with TEA electrolyte.

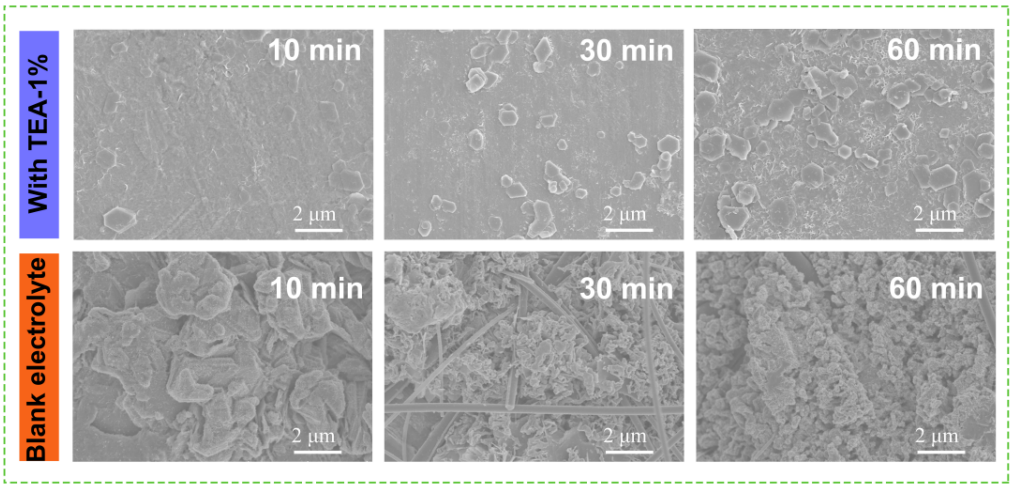

Figure S11. SEM images of the deposited Zn on the Zn substrate after plating for different times at the current density of 6 mA cm^{-2}.

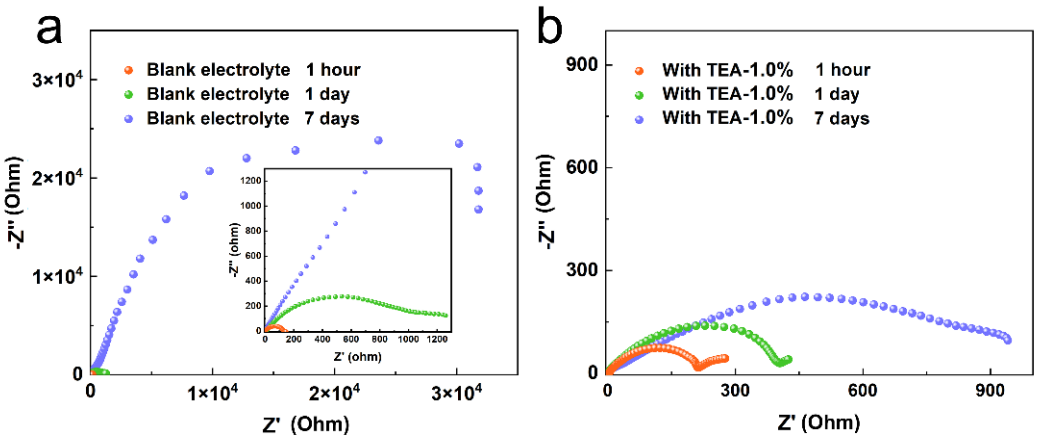

Figure S12. EIS spectra of the Zn anode after immersing for different times in (a) Black electrolyte and (b) TEA-1.0% electrolyte.

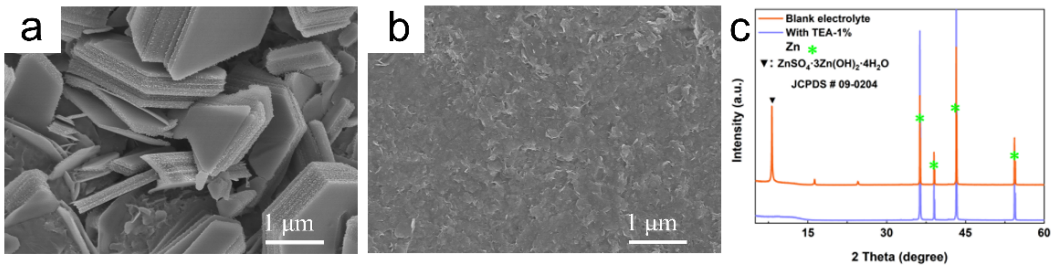

Figure S13. Characterization of the Zn anode after immersion in electrolytes: SEM images of Zn foil extracted from (a) black electrolyte and (b) TEA-1.0% electrolyte and (c) the corresponding XRD patterns.

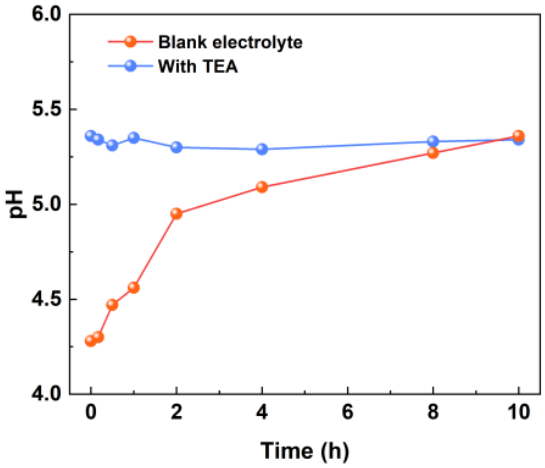

Figure S14. The pH change of Black electrolyte and TEA-1.0% electrolyte during the deposition process at a current density of 1 mA cm^{-2}.

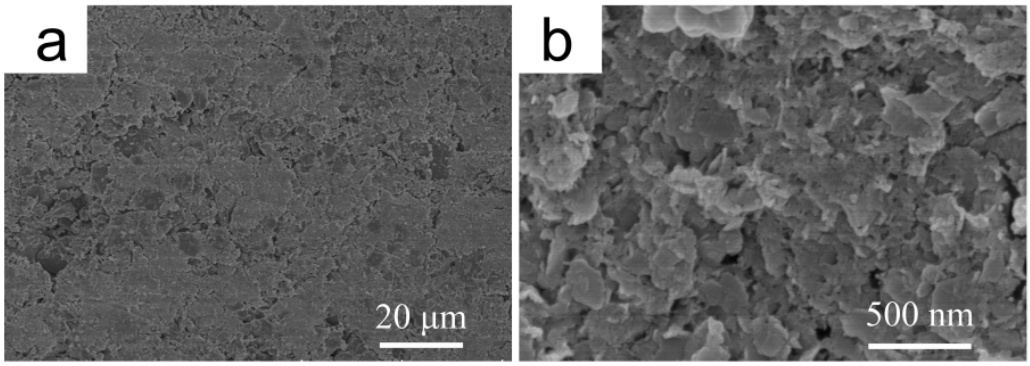

Figure S15. SEM images of the Zn anode after 50 cycles in the electrolyte with 0.5%-TEA additive at the current density of 1.0 mA cm^{-2} with the areal capacity of 1.0 mAh cm^{-2}.

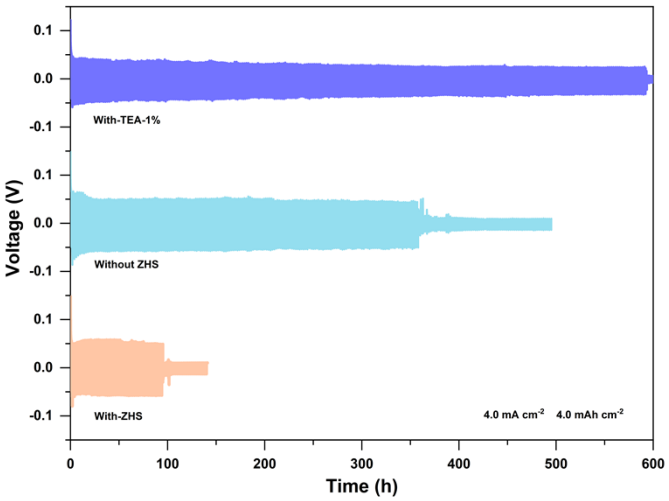

Figure S16. Cycling performance of the symmetric cells with single SEI layer and hybrid SEI layer at the current density of 4.0 mA cm^{-2} with the areal capacity of 4.0 mAh cm^{-2}.

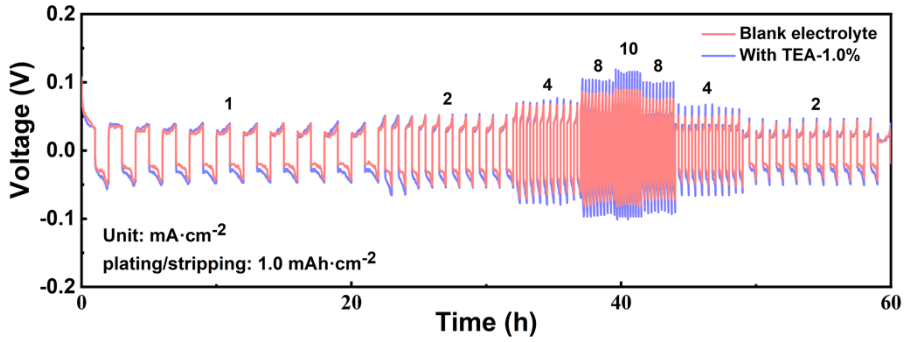

Figure S17. Rate performance of the symmetric cells in blank and TEA-1.0% electrolyte ranging from 1 mA cm^{-2} to 10 mA cm^{-2}.

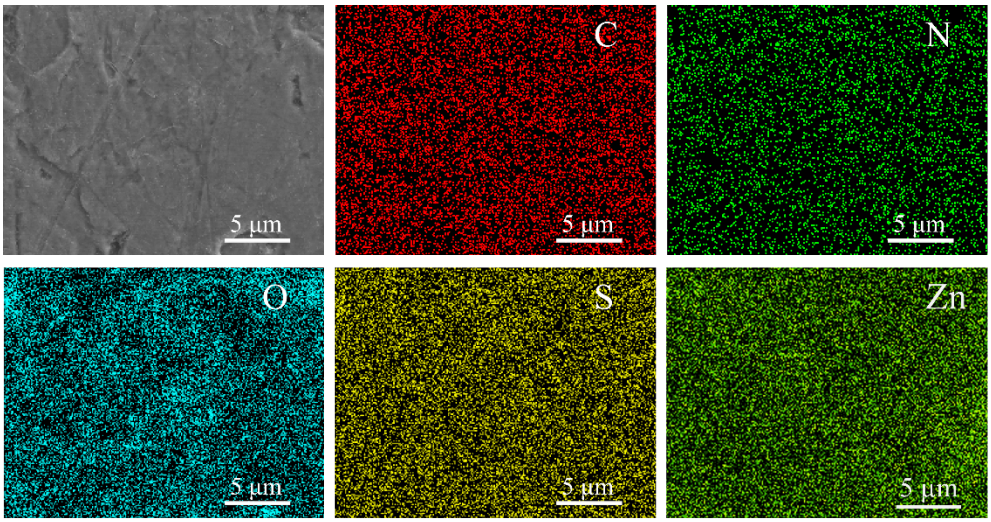

Figure S18. EDS mapping of the Zn anode after 50 cycles in the TEA-1.0% electrolyte at the current density of 1.0 mA cm^{-2} with the areal capacity of 1.0 mAh cm^{-2}.

Table S1. Lifespan comparison between this work and recently published studies.

Zn host	**Current density & Capacity (mA cm^{-2} & mAh cm^{-2})**	**Cycle time (h)**	**Accumulation capacity (mAh cm^{-2})**	**Ref.**
Sn-PCH@Zn	1 &1	750	750	16
PFSA@Zn	1 &1	800	800	17
MCM41@Zn	1 &1	1800	1800	18
PVB@Zn	0.5&0.5	550	275	19
Ag@Zn	5 &5	110	550	20
PVDF/CNTs-PT@ Zn	1 &1	1100	1100	21
PVDF-Sn@Zn/	1 &1	1200	1200	22
3DP-BU@Zn	1 &1	630	630	23
Gr@Zn	0.5&0.5	2500	1250	24
TW-ZHS@Zn	1 &1	1500	1500	25
ZHS@Zn	1 &0.5	2000	2000	26
DFA@Zn	1 &1	1100	1100	27
Zn@ZSH/TEAH^{+}	1 &1	2500	2500	This work

References

1 X. Gan, J. Tang, X. Wang, L. Gong, I. Zhitomirsky, L. Qie and K. Shi, *Energy Storage Materials.* 2023**, 59**, 102769.
2 J. VandeVondele, M. Krack, F. Mohamed, M. Parrinello, T. Chassaing and J. Hutter, *Computer Physics Communications.* 2005**, 167**, 103-128.
3 J. P. Perdew, K. Burke and M. Ernzerhof, *Physical Review Letters.* 1996**, 77**, 3865-3868.
4 S. Grimme, J. Antony, S. Ehrlich and H. Krieg, *The Journal of Chemical Physics.* 2010**, 132**, 154104.
5 S. Grimme, S. Ehrlich and L. Goerigk, *Journal of Computational Chemistry.* 2011**, 32**, 1456-1465.
6 J. VandeVondele and J. Hutter, *The Journal of Chemical Physics.* 2007**, 127**, 114105.
7 S. Goedecker, M. Teter and J. Hutter, *Physical Review B.* 1996**, 54**, 1703-1710.
8 C. Hartwigsen, S. Goedecker and J. Hutter, *Physical Review B.* 1998**, 58**, 3641-3662.

9 S. Grimme, A. Hansen, S. Ehlert and J.-M. J. T. J. o. C. P. Mewes, *The Journal of Chemical Physics.* 2021**, 154**, 064103.
10 M. Gawron, F. Gilch, D. Schmidhuber, J. A. Kelly, T. M. Horsley Downie, A. Jacobi von Wangelin, J. Rehbein and R. Wolf, *Angewandte Chemie International Edition.* 2024**, 63**.
11 N. Mardirossian and M. Head-Gordon, *Physical Chemistry Chemical Physics.* 2014**, 16**, 9904-9924.
12 F. Weigend and R. J. P. C. C. P. Ahlrichs, *Phys. Chem. Chem. Phys.* 2005**, 7**, 3297-3305.
13 A. Mirzanejad and S. A. J. P. C. C. P. Varganov, *Phys. Chem. Chem. Phys.* 2022**, 24**, 20721-20727.
14 F. Neese, F. Wennmohs, A. Hansen and U. J. C. P. Becker, *Chem. Phys.* 2009**, 356**, 98-109.
15 F. Weigend, Physical Chemistry Chemical Physics. 2006**, 8**, 1057-1065.
16 J.-L. Yang, P. Yang, W. Yan, J.-W. Zhao and H. J. Fan, *Energy Storage Mater.* 2022**, 51**, 259-265.
17 L. Hong, X. Wu, L.-Y. Wang, M. Zhong, P. Zhang, L. Jiang, W. Huang, Y. Wang, K.-X. Wang and J.-S. Chen, *ACS Nano.* 2022**, 16**, 6906-6915.
18 Z. Miao, F. Zhang, H. Zhao, M. Du, H. Li, H. Jiang, W. Li, Y. Sang, H. Liu and S. Wang, *Adv. Funct. Mater.* 2022**, 32**, 2111635.
19 S. Wang, Z. Yang, B. Chen, H. Zhou, S. Wan, L. Hu, M. Qiu, L. Qie and Y. Yu, *Energy Storage Mater.* 2022**, 47**, 491-499.
20 X. Zhou, B. Wen, Y. Cai, X. Chen, L. Li, Q. Zhao, S. L. Chou and F. Li, *Angew. Chem. Int. Ed.* 2024**, 63**, e202402342.
21 J. Wang, J. Peng, W. Huang, H. Liang, Y. Hao, J. Li, H. Chu, H. Wei, Y. Zhang and J. Liu, *Adv. Funct. Mater.* 2024**, 34**, 2316083.
22 Q. Cao, Y. Gao, J. Pu, X. Zhao, Y. Wang, J. Chen and C. Guan, *Nat. Commun.* 2023**, 14**, 641.
23 H. He, L. Zeng, D. Luo, J. He, X. Li, Z. Guo and C. Zhang, *Adv. Mater.* 2023**, 35**, 2211498.
24 Y. Zou, Y. Wu, W. Wei, C. Qiao, M. Lu, Y. Su, W. Guo, X. Yang, Y. Song, M. Tian, S. Dou, Z. Liu and J. Sun, *Adv. Mater.* 2024**, 36**, 2313775.
25 K. Huang, X. Zeng, D. Zhang, Y. Wang, M. Lan, C. Wen and Y. Guo, *Nano Res.* 2024**, 17**, 5243-5250.
26 W. Yuan, G. Ma, X. Nie, Y. Wang, S. Di, L. Wang, J. Wang, S. Shen and N. Zhang, *Chem. Eng. J.* 2022**, 431**, 134076.
27 H. Tian, J. L. Yang, Y. Deng, W. Tang, R. Liu, C. Xu, P. Han and H. J. Fan, *Adv. Energy Mater.* 2022**, 13**, 2202603.